Spatial Constraint-Based Navigation and Emergency Replanning Adaptive Control for Magnetic Helical Microrobots in Dynamic Environments

Shihao Zhong, Yaozhen Hou, Qing Shi, *Senior Member, IEEE*, Yang Li, Hen-Wei Huang, Qiang Huang, *Fellow, IEEE*, Toshio Fukuda, *Life Fellow, IEEE*, and Huaping Wang, *Member, IEEE*

***Abstract*— Magnetic helical microrobots have attracted considerable attention in navigation control. However, the performance of microrobots is negatively affected by time-varying uncertain perturbations and obstacles, at the microscale. In this study, we present a navigation control scheme for accurately guiding the helical microrobot to targeted positions in dynamically changing environments. To efficiently plan smooth paths, a search-based algorithm with pruning rules is implemented to quickly find collision-free waypoints and design an optimal method with spatial and dynamic constraints for obtaining smooth paths globally. Velocity gain and potential fields are integrated to develop an emergency local motion replanning method for addressing random obstacles that suddenly appear in the preset path. In order to attain microrobot system dynamic linearization and achieve precise path following of a helical microrobot, a robust control strategy that integrates geometric and model-free controllers in a complementary manner is presented. The geometric controller as a feedforward controller, responsible for managing path information and generating guidance laws. In contrast, the model-free controller operates as a feedback controller, specifically designed to rapidly address position deviation. Meanwhile, we employ an observer to compensate for disturbances. Experimental results of precise motion control in both static and dynamic environments demonstrate the effectiveness of this navigation control scheme, which is promising for moving with high accuracy in cluttered and dynamic living enclosed environments.**

***Note to Practitioners*—This paper was motivated by the problem of the navigation control of magnetic microrobots in dynamic environment. The existing navigation control methods of microrobots mainly focus on the static environment, which is challenging to meet the emergency obstacle avoidance requirements in the cluttered environment with low Reynolds number. In addition, the conventional path following control always ignores the nonlinearity of the microrobot system, resulting in insufficient following accuracy. In this work, a novel navigation control method for microrobots is proposed, which can guide microrobots to accurately follow dynamically planned paths in cluttered environments without collision. Simulations and experiments validate the performance of the proposed navigation control method using helical microrobots. The proposed navigation control method paves the way for a better understanding of advanced navigation control method for magnetic microrobots.**

***Index Terms*— Magnetic helical microrobot, nonholonomic motion control at microscales, electromagnetic actuation, motion planning, adaptive control.**

I. Introduction

MICRON-SIZED helical robots that can be remotely controlled by magnetic fields have garnered considerable interest due to their potential for transformative biomedical applications, as these robots have the ability to access difficult-to-reach enclosure regions inside the human body [1], [2], [3], [4], [5], [6]. However, guiding a helical microrobot to a specific target location (e.g., tumor, thrombus) while avoiding obstacles in a dynamic cluttered environment is immensely challenging [7], [8], [9], [10]. This requires the microrobot system to not only plan and execute collision-free and dynamically feasible paths but also move toward the path with high precision.

The initial stage of the dynamic path-planning procedure involves identifying a sequence of waypoints through utilizing either randomized or search-based algorithms [11]. Due to their inherent random planning behavior, randomized path-planning methods such as RRT and PRM exhibit unpredictable performance when requiring frequent replanning or when operating in confined and narrow environments [12]. As resolution-complete methods, search-based path-planning approaches such as Dijkstra and A* can plan viable paths

Manuscript received 29 October 2023; accepted 2 December 2023. Date of publication 20 December 2023; date of current version 16 October 2024. This article was recommended for publication by Associate Editor T. Xu and Editor L. Zhang upon evaluation of the reviewers' comments. This work was supported in part by the National Key Research and Development Program of China under Grant 2023YFB4705400; in part by the National Natural Science Foundation of China under Grant 62073042, Grant 62222305, and Grant U22A2064; in part by the Beijing Natural Science Foundation under Grant 4232055; and in part by the Science and Technology Innovation Program of Beijing Institute of Technology under Grant 2022CX01019. *(Corresponding author: Huaping Wang.)*

Shihao Zhong and Yaozhen Hou are with the Intelligent Robotics Institute, School of Mechatronical Engineering, Beijing Institute of Technology, Beijing 100081, China (e-mail: 3120235409@bit.edu.cn; 7520230117@bit.edu.cn).

Qing Shi, Qiang Huang, and Toshio Fukuda are with the Beijing Advanced Innovation Center for Intelligent Robots and Systems, Beijing Institute of Technology, Beijing 100081, China (e-mail: shiqing@bit.edu.cn; qhuang@bit.edu.cn; tofukuda@nifty.com).

Yang Li is with Peking University First Hospital, Xicheng, Beijing 100034, China (e-mail: liy95279527@163.com).

Hen-Wei Huang is with the Laboratory for Translational Engineering, Harvard Medical School, Cambridge, MA 02139 USA (e-mail: hhuang27@bwh.harvard.edu).

Huaping Wang is with the Key Laboratory of Biomimetic Robots and Systems, Beijing Institute of Technology, Ministry of Education, Beijing 100081, China (e-mail: wanghuaping@bit.edu.cn).

This article has supplementary material provided by the authors and color versions of one or more figures available at https://doi.org/10.1109/TASE.2023.3339637.

Digital Object Identifier 10.1109/TASE.2023.3339637

in complex environments. However, the considerable increase in the number of nodes may reduce the planning efficiency [13]. Therefore, efficient planning of a feasible path for a helical microrobot in a heterogeneous liquid environment with multiple obstacles remains an open area of research. After identifying a sequence of waypoints, the resulting path may be convoluted and nonsmooth in form, causing a sudden change in motion states at turning points and consequently hindering the stability of the microrobot. Thus, the straight-line rough paths must be optimized for smoothness to ensure that the motion of the helical microrobots changes less abruptly and more gently. The path optimization problem is commonly transformed into a constrained quadratic programming (QP) problem [14], which is widely used in the field of unmanned aerial vehicles. In scenarios with multiple obstacles, the optimized path may deviate significantly from the original path and may even intersect with obstacles, thereby increasing the risk of collision. Therefore, smoothness and safety constraints (spatial constraints) must be considered simultaneously. Furthermore, the microscale liquid environment is subject to dynamic changes influenced by factors such as heterogeneity, thermal noise, and Brownian motion [15], [16], [17]. Unknown suspended objects can suddenly become dynamic obstacles that unexpectedly enter the microrobot's field of view and unpredictably approach the microrobot. Therefore, by avoiding local random obstacles when responding to emergencies during global path planning, the motion robustness of microrobots can be effectively improved.

To accurately follow the dynamically planned path, the path-following controller must quickly address any offset errors. However, in a dynamic microenvironment, the helical microrobot system exhibits high nonlinearity, causing the robots to deviate frequently from their intended state [18], [19], [20]. To actuate the helical microrobot, the controller continuously adjusts the direction and magnitude of the current flowing into the electromagnet to produce a corresponding control magnetic field. However, due to the inherent hysteresis and input saturation characteristics of the nonlinear electromagnetic drive system, the rate of change of the magnetic field lags behind that of the control command, and the strength of the magnetic field may not match the desired value [21]. A common control method for nonlinear microrobot systems involves linearizing the dynamic model by ignoring higher-order disturbance terms and reducing deviation by artificially adjusting the control parameters [22]. As a result, managing sudden deviations in the helical microrobot system can be difficult, causing the movement to become uncontrollable. If unmodeled system dynamics and random disturbances can be estimated and compensated for or even eliminated, the nonlinear microrobot system can be approximated as linear, significantly reducing the control difficulty. Common motion control methods for linearized microrobot actuate systems currently include geometric controllers, model-based controllers, and model-free controllers. Geometric methods [23], [24] rely heavily on the geometric relationship to calculate the direction of movement while being unable to directly address tracking errors. Model-free control methods [25], [26] are overly sensitive to feedback errors at each time step, making ensuring high system stability difficult. Model-based and optimization-based methods [5], [27] achieve path-following through continuous iterative calculations, the tracking performance of these methods greatly dependent on the accuracy of the dynamic model. However, it is challenging to obtain high-fidelity models at the microscale. They also consume large amounts of computational resources. Overall, the aforementioned methods are unable to address every aspect of the tracking process and cannot ensure tracking performance and system stability. When situations get more complicated, the performance of above methods may decline significantly, or they may even become ineffective due to their inability to account for unknown factors. Therefore, a method that divides the path-following tasks of microrobots into multiple subtasks and controls them independently, greatly improving path-following performance, is needed.

In this study, we present a navigation control scheme to design collision-free and dynamically viable paths for a helical microrobot with high path-following precision. To efficiently plan a smooth path, a search-based algorithm with pruning rules is implemented to quickly find collision-free waypoints and then design an optimal method with spatial and dynamic constraints for obtaining a globally smooth path. By integrating velocity gain and potential fields, an emergency local motion replanning method is developed to address random obstacles that suddenly appear in the preset path. In order to attain system dynamic linearization and achieve precise path following task, a robust motion control method that integrates geometric and model-free controllers in a complementary manner is proposed. The geometric controller is employed as a feedforward method to handle path information and formulate guidance laws, whereas the model-free controller is utilized as a feedback method to rapidly respond to position deviation. Additionally, an extended state observer (ESO) is utilized to compensate for unmodeled dynamics and unknown disturbances in our approach. Simulation and experimental results of following arbitrary paths and handling with dynamic environments demonstrate the significant potential of this navigation control method for dealing with complicated conditions.

The paper is structured as follows. Section II describes the motion model; Section III presents the navigation and control method; Section IV presents the electromagnetic actuation setup; Section V shows the simulation and experimental results, and this paper is concluded in Section VI.

II. Path-Following Problem Formulation

A. The Movement Model

The schematic diagram of the electromagnetic workspace is shown in Fig. 1(a), where $e_i (i = 1 \cdots 8)$ denotes the center position of the i electromagnetic coil. The dimensions of the working space are shown in Table I. The basic coordinate O_b and the image coordinate O_i are established. As shown in Fig.1(b), $q = [x(t), y(t)]^T$ is denoted the position with respect to the basic coordinate. $p = [p_x(t), p_y(t)]^T$ is denoted the position with respect to the image coordinate.

Assuming a no-slip boundary condition at low Re, the Stokes equations require that there exists a linear relationship

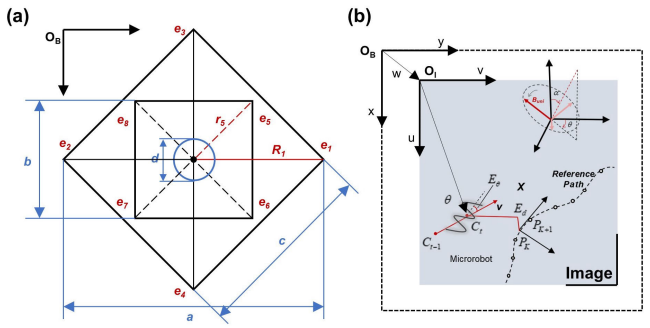

Fig. 1. (a) Structural diagram of the electromagnetic workspace. (b) Motion diagram of helical microrobot.

TABLE I
DIMENSIONS OF THE WORKSPACE (MM)

Dimension	Value	Dimension	Value	Dimension	Value
a	147	c	104	R	73.5
b	52.5	d	42	r	37.1

between the speed and rotational frequency of the propeller motion, and the externally nonfluidic applied force and torque, which means when an external force and an external torque are applied to the helical microrobot, it moves with linear velocity and angular velocity [1]. For generalization, we think of microrobots as mass dot motion. In a liquid environment characterized by a significantly low Reynolds number (Re), a helical structure has the capability to be propelled by a uniformly rotating field. But, when it comes to performing tasks at the microscale in such liquid environments, locomotive devices encounter considerable diffusivity caused by disturbances. In addition, the spin top motion, which relies on friction, enables the helical microrobot to make contact with the surface solely at its tip, ensuring efficient and effective movement. However, obtaining the dynamics of the spin top motion can be difficult. Hence, we consolidate the unmodeled dynamic behavior and time-varying disturbances into a generalized disturbance. In addition, due to the low Re effect, the acceleration of the microrobot is negligible. Therefore, the motion model of the microrobot is:

$$\begin{cases} \dot{P}_x = g_x(t) + D_x \\ g_x = F(f,\alpha)\cos(\alpha)\cos(\theta) \\ \dot{P}_y = g_y(t) + D_y \\ g_y = F(f,\alpha)\cos(\alpha)\sin(\theta) \end{cases} \tag{1}$$

where $g_{x,y}$ represent the expected velocity of the helical microrobot in the X and Y directions, respectively. f represents the rotation magnetic field frequency. α and θ represent the pitch and yaw angles, respectively. $F(f,\alpha)$ is a nonlinear function representing the velocity of the microrobot, and its value is related to the pitch and the rotation frequency. $D_{x,y}$ are unknown disturbances.

B. Image-Based Visual Servo Path Following

The path following task of helical microrobot is realized based on visual servo. The task objective includes eliminating distance error and yaw error, as shown in Fig.1(b). We set the desired arbitrary path as a series of waypoints $P_d(K) = [x_d(K), y_d(K)]$. The expected path is discretized to select a section K_{th}, which the beginning point is P_K and the terminate point is P_{K+1}. The current center of mass of the microrobot is C_t, and the center of mass of the previous moment is C_{t-1}. D_K is the projection of C_t onto the segment $L^{P_K}_{P_{K+1}}$. Therefore, distance error E_d and yaw error E_θ are expressed by the formulas (2) and (3).

$$E_d = C_t D_K = \frac{L^{P_K}_{P_{K+1}} \times L^{C_t}_{P_k}}{\left\| L^{P_K}_{P_{K+1}} \right\|^2} L^{P_K}_{P_{K+1}} - L^{D_K}_{p_k} \tag{2}$$

$$E_\theta = \cos^{-1} \frac{L^{P_K}_{P_{K+1}} \bullet L^{C_{t-1}}_{C_t}}{\left\| L^{P_K}_{P_{K+1}} \right\| \left\| L^{C_{t-1}}_{C_t} \right\|} \tag{3}$$

III. MOTION PLANNING AND CONTROL DESIGN

This motion planner aims to generate a smooth and obstacle-free path. The jump point search (JPS) algorithm [13] is initially employed to find a preliminary path, which is then optimized using the minimum jerk method within a safe travel corridor [28] and under kinematic constraints. In situations where the helical microrobot encounters randomly appearing obstacles or other challenges during motion, a novel improved artificial potential function algorithm is developed for local obstacle avoidance.

The control loop of the helical microrobot incorporates two main modules. (I) An ESO [26] is used to suppress generalized disturbances, making the nonlinear system dynamic able to be approximated by linearization. (II) A combination control model of the geometric method (pure pursuit with the line-of-sight method (PLOS) [29]) and model-free method (PID) handles path information and position error to achieve accurate path following.

A. Trajectory Generation

1) Initial Path Generation: In motion planning tasks, the environment is commonly modeled using an occupancy grid, which can be created through the use of sensor data such as camera feeds. To accommodate the actual dimensions of the helical microrobot system, each new obstacle point is expanded into a cubic volume of fixed size upon being inserted into the map. In the initial stage, a passable waypoint path free of collisions can be identified using the JPS path planner. The JPS method is combines A* search with specific pruning rules that reduce the runtime of A* by an order of magnitude. As defined in [13], the term "natural neighbors" refers to the remaining set of nodes after the pruning process. On the other hand, neighbors that cannot be pruned due to the presence of nearby obstacles are known as "forced neighbors." The cost function adopted in the proposed methodology bears resemblance to that of the A* algorithm. Specifically, the heuristic function is defined as the Euclidean distance between the current node and the intended destination node, while the cost function is defined as the Euclidean distance between the current node and its parent node.

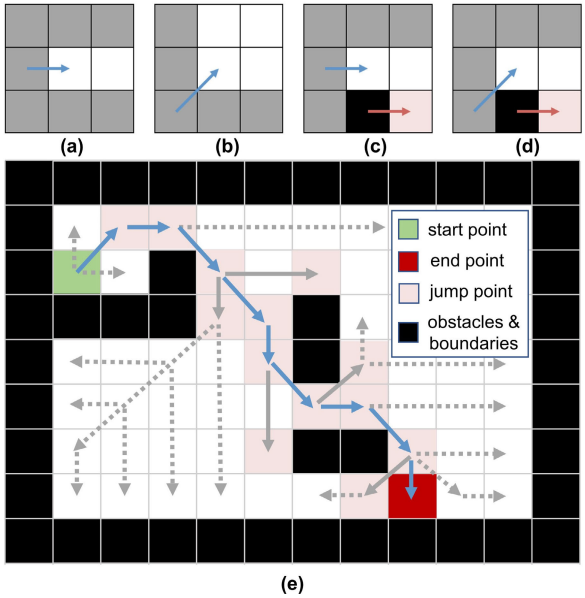

Fig. 2. (a)-(d) Neighbor pruning rules of the JPS method. The natural neighbors of the current node are highlighted in white. The pruned neighbors are marked gray. The blue arrow also shows the direction from the parent. When the current node is adjacent to an obstacle (depicted in black), it is crucial to note that the highlighted forced neighbors (shown in pink) should not be pruned. The red arrow denotes the pairing between an obstacle and its respective forced neighbor. (e) Path found by the JPS method (blue arrow line). The gray line represents the search process.

The fundamental concept behind the JPS method involves expanding from the starting point and selecting the jump point with the lowest cost from among the natural neighbors as the next node for expansion. This process is repeated until the endpoint is reached. If a path is found upon completion of the loop, the path can be recorded. Fig. 2 illustrates a complex path through a maze.

2) Corridor Generation and Path Optimization: The path found by the JPS method is composed of multiple straight lines, which may result in infeasible and inefficient motion due to the constraints of the system dynamics, such as the speed of the microrobots and the change in speed of the microrobots. Hence, the route should be optimized to enhance the caliber and temporal efficiency. The newly generated path can be mathematically represented as a multisegment polynomial, and its optimization problem can be formulated as a quadratic programming (QP) problem [24]. N new waypoints along the specified path are sampled evenly in the time horizon, and intermediate waypoints are added at a distance from the obstacle boundary to prevent collisions with the obstacle.

A series of corridors are generated to cover the waypoints generated by the JPS method. The principle of determining the k_{th} safe travel corridor is introduced as follows.

$$\begin{aligned} &x_{\min} \le x_d(k) \le x_{\max},\ y_{\min} < y_d(k) \le y_{\max} \\ &s.t. \frac{3}{4} l_{robot} < x_{\max} - x_{\min},\ y_{\max} - y_{\min} < \frac{3}{2} l_{robot} \end{aligned} \tag{4}$$

where l_{robot} denotes the helical microrobot major axis length.

The M-segment, N^{th} order piecewise polynomial path is designed to ensure a smooth passage through the waypoints within specified corridors. By considering the start time of the path and all end-times of individual segments, one dimension of the entire path can be expressed as follows:

$$M(t) = \begin{cases} \sum_{j=0}^{N} n_{1j}(t-t_0)^j, & t_0 \le t \le t_1 \\ \sum_{j=0}^{N} n_{2j}(t-t_1)^j, & t_1 \le t \le t_2 \\ \vdots & \\ \sum_{j=0}^{N} n_{Mj}(t-t_{M-1})^j, & t_{M-1} \le t \le t_M \end{cases} \tag{5}$$

where n_{ij} is the j^{th} order polynomial coefficient of the i^{th} path segment.

Both corridor and dynamical constraints can be formulated either as linear equality ($A_{eq}p = b_{eq}$) or inequality ($A_{lq}p \le b_{lq}$) constraints. The object function (5) can be expressed as p^THp, where p represents the vector of polynomial coefficients for all segments and H denotes the Hessian matrix. Hence, path generation can be effectively represented as a quadratic programming problem.

$$\begin{aligned} &\min p^THP \\ &\text{s.t. } A_{eq}p = b_{eq} \\ &\quad A_{lq}p \le b_{lq} \end{aligned} \tag{6}$$

In order to achieve a smooth transition between path segments, we ensure continuity of the first $N_\phi - 1$ derivatives at the times when segment transitions occur.

The optimization objective is to find a path that minimizes the integral of the square of the N_ϕ^{th} derivative, which can be expressed as:

$$\min \int_{t_0}^{t_M} \left(\frac{d^{N_\phi} f(t)}{dt^{N_\phi}} \right)^2 dt \tag{7}$$

In this paper, we set a specific value $N_\phi = 3$ and aim to minimize the total jerk of the polynomial path. Minimizing the total jerk of the polynomial path not only ensures path smoothness, but also results in reduced acceleration changes and, by extension, decreased current variations in the electromagnetic system. This can effectively mitigate the negative effects of coil hysteresis.

To make the optimized path $M(t)$ as close as possible to the preset path $M_d(t)$, we add a guiding error with a regular coefficient:

$$\min \int_{t_0}^{t_M} \left(\frac{d^{N_\phi} f(t)}{dt^{N_\phi}} \right)^2 dt + \lambda \int_{t_0}^{t_M} (\| f(t) - f_d(t) \|)^2 dt \tag{8}$$

where λ is a nonnegative constant that can adjust the balance between path smoothness and target curve tracking. The larger λ is, the closer the optimized path is to the preset path (see Fig. 3).

B. Improved Artificial Potential Function Method

Artificial fields, generated by obstacles and the goal potential, are considered as potential functions (PFs) that serve to

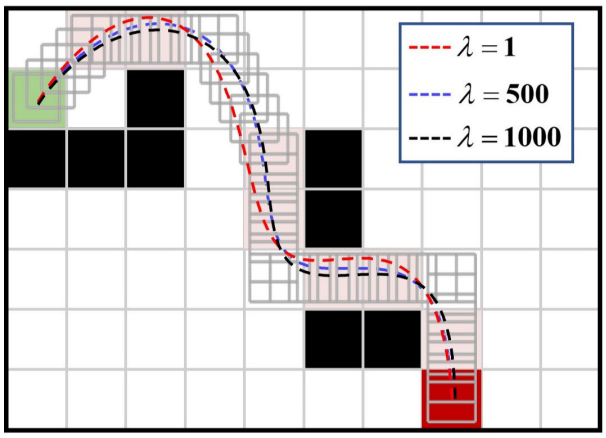

Fig. 3. The optimized paths diagram. The gray boxes represent corridors. The green, red, and pink boxes represent the start, end, and jump points, respectively. The black boxes represent the inflated obstacles.

direct the helical microrobot towards the goal while simultaneously ensuring safe distance from obstacles [30]. The goal PF features a minimum at the goal position, enabling it to attract the helical microrobot towards the desired destination. Conversely, the obstacle PF exhibits a maximum at the obstacle's position, creating a repulsive force that helps the helical microrobot avoid collisions. However, traditional artificial potential field (APF) algorithms often encounter challenges related to local minima and oscillations. To address these issues, a novel Improved Artificial Potential Field (IAPF) algorithm is developed specifically for emergency path replanning of helical microrobots within constrained spaces.

In the event of an obstacle within the field of view, the motion control program automatically transitions to the IAPF processing module. The helical microrobot will experiences the repulsive forces from the obstacles and the attractive force from the target. Hence, the helical microrobot should navigate in the direction of the resultant force. The APF can be defined as follows:

$$U = U_a + \sum_{i=1}^{m} U_r \tag{9}$$

$$U_a(q) = \frac{1}{2} k_a \|q - q_t\|^2 \tag{10}$$

$$U_r(q) \begin{cases} \frac{1}{2} k_r \left(\frac{1}{\|q - q_o\|} - \frac{1}{\lambda} \right)^2, & \|q - q_t\| \le \lambda_o \bigcap \angle q q_o > 0 \\ 0, & otherwise \end{cases} \tag{11}$$

where U_a denotes the attractive potential, U_r signifies the repulsive potential, and m represents the number of obstacles encountered in the system. $k_{a,r}$ are positive coefficients. q_t denotes the target location. q_o denotes the obstacle location. $\|\cdot\|$ is the distance operation. λ_o denotes the maximum impact range of obstacles.

The artificial force that acts on the microrobot is described as being the negative gradient of the APF. This force is given

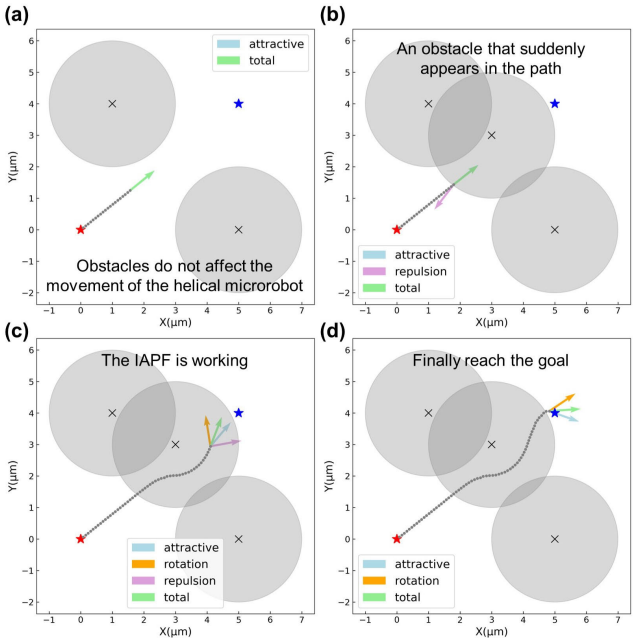

Fig. 4. Diagram of the local random obstacle avoidance based on the IAPF. Red and blue stars represent the start and end points, respectively.

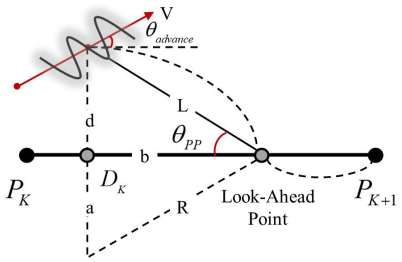

Fig. 5. The geometry of the pure pursuit with LOS-based path following.

by the following expression:

$$F = -\nabla U = -\nabla U_a - \nabla \sum_{i=1}^{m} U_r = F_a + \sum_{i=1}^{m} F_r \tag{12}$$

where F_a is the attractive force and F_r is the repulsive force. When $F_a \neq 0$, $\sum_{i=1}^{m} F_r \neq 0$, while $F \approx 0$ and means that F_a and F_r have the same magnitude in opposite directions. This results in the local minima and oscillations problem, that is, the helical microrobot becomes stuck. To address this, inspired by [30], a rotating potential force F_s is added to the artificial force as follows:

$$F_s = \begin{cases} k_s T_R \dfrac{q - q_t}{\|q - q_t\|}, & \text{if object is stuck} \\ 0, & \text{otherwise} \end{cases} \tag{13}$$

where k_s is a positive coefficient. T_R is a rotation matrix for which the rotation angle belongs to $(0, 90]$.

When the microrobot must achieve random avoidance, the new local obstacle avoidance algorithm is regarded as

$$u_i = F_a + \sum_{i=1}^{m} F_r + F_s - kv \tag{14}$$

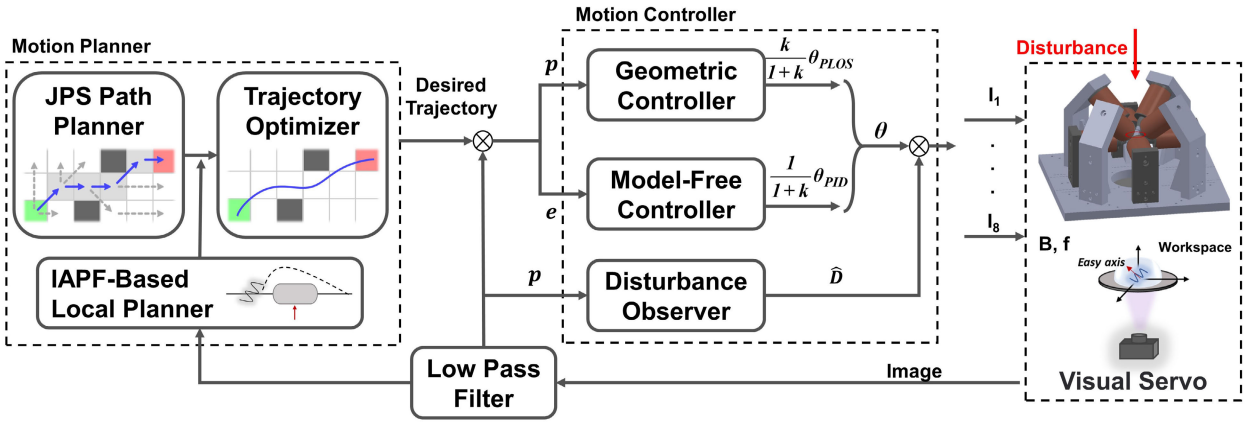

Fig. 6. Block diagram of the navigation control system of the helical microrobot system.

where k is a positive control gain used for damping. v is the velocity of the helical microrobot. Under the assumption of bounded control signals, the proposed control law facilitates the microrobot to approach the target in an asymptotic and collision-free manner. The simulation results of emergency obstacle avoidance for microrobots based on IAPF algorithm are shown in Fig. 4.

C. Controller Design

1) Disturbance Observer: As the environment changes dynamically at a microscale, estimating and compensating for the environmental noise is necessary. When the measurement noise existed, the linear ESO is typically considered superior to nonlinear one in terms of performance and robustness [31]. The observer is represented by the formula (15).

$$\begin{cases} \dot{\hat{a}}_1(t) = \hat{a}_2(t) + g_x(t) + \lambda_1(p_x(t) - \hat{a}_1(t)) \\ \dot{\hat{a}}_2(t) = \lambda_2(p_x(t) - \hat{a}_1(t)) \\ \dot{\hat{a}}_3(t) = \hat{a}_3(t) + g_y(t) + \lambda_3\big(p_y(t) - \hat{a}_3(t)\big) \\ \dot{\hat{a}}_4(t) = \lambda_4\big(p_y(t) - \hat{a}_3(t)\big) \end{cases}$$

$$\begin{aligned} s.t. \\ a(t) &= [a_1(t), a_2(t), a_3(t), a_4(t)]^T \\ &= \big[p_x(t), D_x(t), p_y(t), D_y(t)\big]^T \\ \hat{a}(t) &= [\hat{a}_1(t), \hat{a}_2(t), \hat{a}_3(t), \hat{a}_4(t)]^T \\ &= [\hat{p}_x(t), \hat{D}_x(t), \hat{p}_y(t), \hat{D}_y(t)]^T \end{aligned} \tag{15}$$

where $\lambda_i (i = 1, 2, 3, 4)$ denote the positive parameters, $a(t)$ denotes the designed extended system state vector, and $\hat{a}(t)$ denote the state estimation vector.

The error dynamic of the observer is obtained as

$$\dot{e} = Ae + B$$

$$A = \begin{bmatrix} -\lambda_1 & 1 & 0 & 0 \\ -\lambda_2 & 0 & 0 & 0 \\ 0 & 0 & -\lambda_3 & 1 \\ 0 & 0 & -\lambda_4 & 0 \end{bmatrix} B = \begin{bmatrix} 0 \\ -\dot{D}_x(t) \\ 0 \\ -\dot{D}_y(t) \end{bmatrix} \tag{16}$$

If appropriate parameters $\lambda_i (i = 1, 2, 3, 4)$ are selected, A is Hurwitz. In addition, we assume that the derivative of the disturbance in B are bounded. Theoretically, the designed observer is convergent, and the estimation error is bounded.

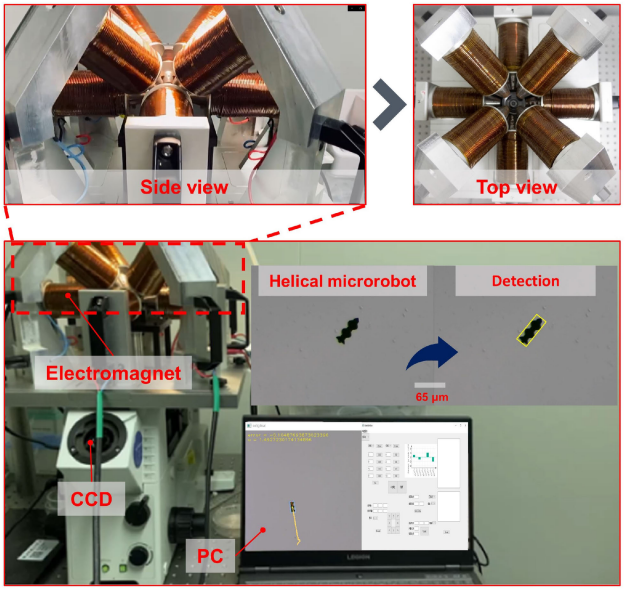

Fig. 7. The Schematic diagram of electromagnetic drive system.

2) PLOS-PID Controller: The path is followed through feedback control to reduce the defined error. The PLOS method is used to formulate the guidance law, which drove the helical microrobot toward the look-ahead point along the path segment. The PID method can rapidly respond to the distance error.

The relationship between the motion state of the helical microrobot and the target path is shown in Fig. 5. In PLOS method, look-ahead distance L is an important factor affecting path following. When the microrobot moves to the target position, the turning radius $R_{turning}$ is the smallest. We can obtain the relationship between L and $R_{turning}$ as follow:

$$L = 2R_{\min} \tag{17}$$

Therefore, the motion control direction of the microrobot is:

$$\theta_{PLOS} = -atan2(d, b) - \theta_{advance} + K_{LOS}d \tag{18}$$

where d is the minimum distance between the microrobot's center of mass and the target path, b is the distance between the

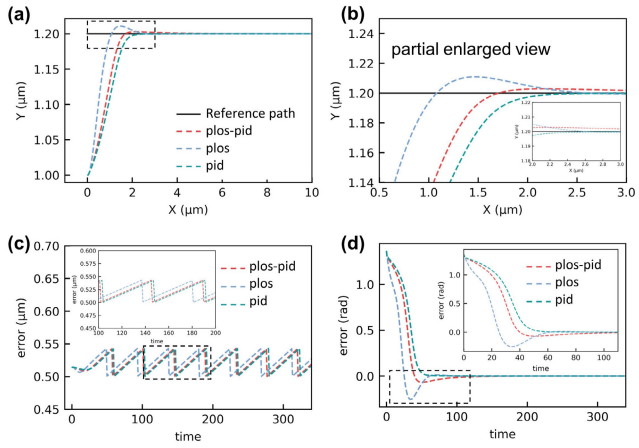

Fig. 8. Linear path simulation results. (a) The diagram of the motion process. (b) The partial enlarge view. (c) Position errors. (d) Steering errors.

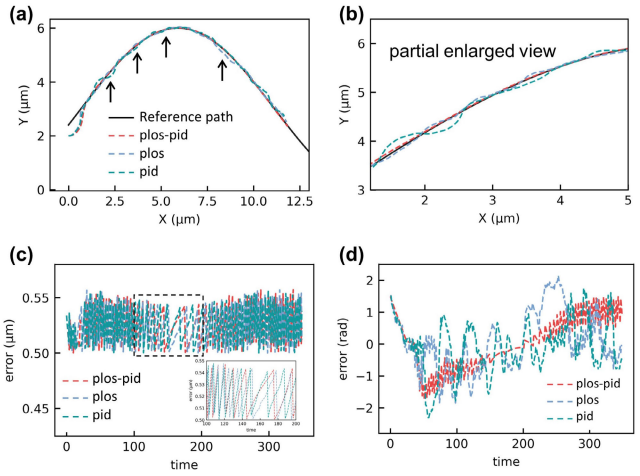

Fig. 9. Curve path simulation results. (a) The diagram of the motion process. (b) The partial enlarge view. (c) Position errors. (d) Steering errors.

projection point of the microrobot's centroid on the path and the look-ahead point, $\theta_{advance}$ is the current motion direction of the robot, and K_{LOS} is the proportional gain.

PID is deployed to intensify the control of feedback tracking error. Parameters e_{la} pertaining to E_d and E_θ are constructed as the feedback value feed to the controller.

$$\theta_{PID} = K_p e_{la}(t) + K_i \int_0^t e_{la}(t) + K_d \frac{de_{la}(t)}{dt} \tag{19}$$

where $e_{la} = E_d + L \sin E_\theta$, and $K_{p,i,d}$ are positive parameters, respectively. if L is not optimized, it leads to an increase in distance error, which is then compensated for by the PID controller.

The PLOS-PID controller is summarized as

$$\theta_{PLOS-PID} = LP(\mu(1+\mu)^{-1}\theta_{PLOS} + (1+\mu)^{-1}\theta_{PID}) \tag{20}$$

where $\theta_{PLOS-PID}$ is the motion control value, μ denotes the weight ratio coefficient of PLOS and PID and $LP(\bullet)$ denotes a filter function.

Combining the ESO and PLOS-PID, the motion control direction of spiral microrobot is

$$\theta_C(t) = \theta_{PLOS-PID} - \widehat{D}(t) \tag{21}$$

where $\hat{D}(t)$ is the estimation vector of the ESO.

IV. System Setup

A. Magnetic Field Generation System

This section outlines the actuation mechanism of the helical microrobot, which features an eight-stage electromagnet system depicted in Fig. 7. The system comprises four horizontally configured stages and four diagonally configured stages. Additionally, an inverted microscope is placed beneath the working area to monitor the movement of the microrobot [32].

The application of a rotating magnetic field on the helical microrobot induces a rotational motion, driving the spin of the microrobot through the exertion of magnetic moment T.

$$T = m \times B \tag{22}$$

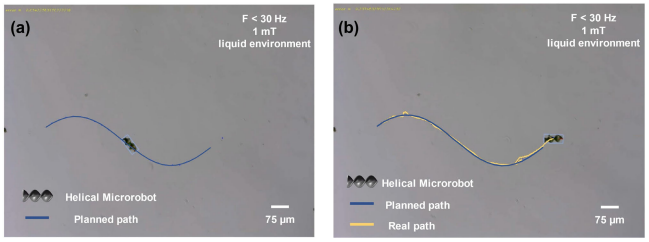

Fig. 10. Schematic diagram of curve path following experimental results.

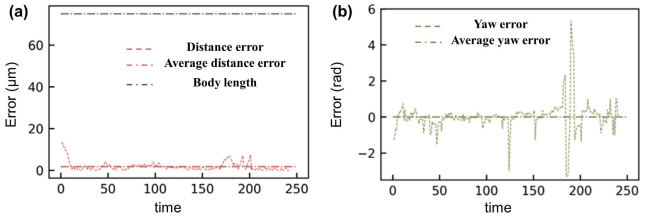

Fig. 11. Schematic diagram of curve path follows experimental error.

where m represents the magnetic moment (A/m^2), and B represents the flux density of the applied field with optimal currents.

When implementing a rotating magnetic field, the flux density B at any time can be calculated in real time by the rotation matrix [33]: (23), as shown at the bottom of the next page, where $C = \cos\varphi$, $S = \sin\varphi$, and φ denotes the step angle. A represents the rotation axis vector. B_{ini} represents the initial flux density vector.

Once the rotating magnetic field vector is obtained around any axis, the corresponding current necessary for each coil can be determined.

B. The Microrobot Structure

The double helix structure is one of the typical helical microrobots [32]. We manufacture the body using biocompatible hydrogels. The hydrogel material is mixed with the photoinitiator and solidified into a helical structure by a two-photon printing device. In addition, the helical microrobot uniformly contains magnetic nanoparticles driven by magnetic fields. The helical microrobot possesses dimensions of 75 μm

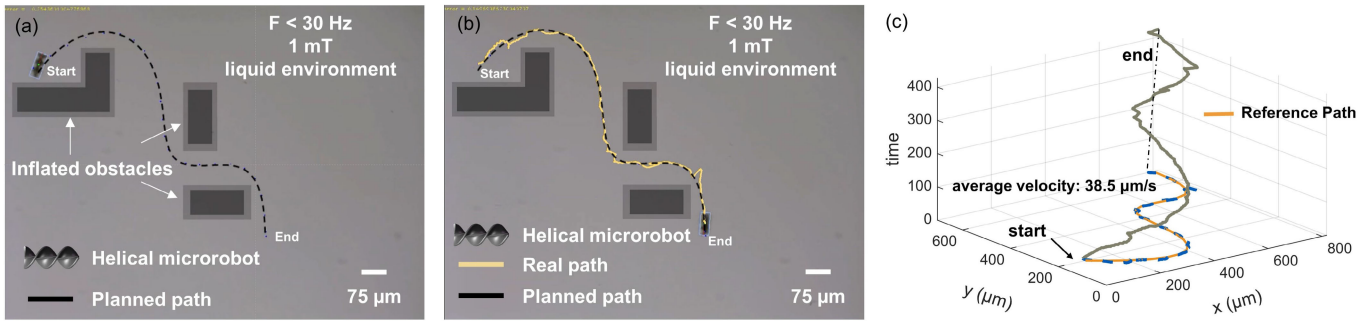

Fig. 12. Experimental results of navigation control in static obstacles map.

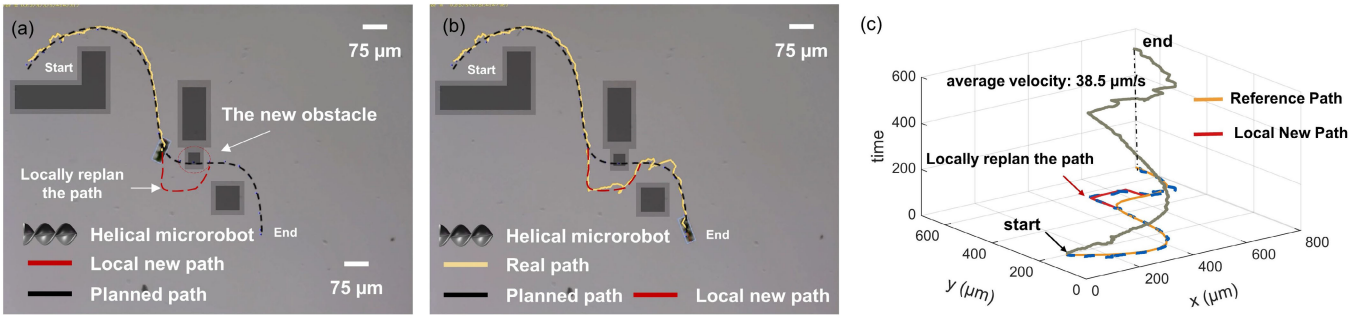

Fig. 13. Experimental results of navigation control in variational obstacles map.

in length, 31 μm in width, and a wavenumber of 1.25. The image of the microrobot is shown in Fig. 7.

The helical microrobots have a cutoff frequency. At frequencies below this threshold, the helical microrobots demonstrate synchronous rotation with the external magnetic field. Moreover, when the rotation frequency remains below the critical value, a linear positive correlation exists between the speed of movement and the rotation frequency under ideal conditions. The movement speed rapidly declines when the rotation frequency is over the critical value. Too high or too low rotation frequencies produce varying degrees of wobbling motion. In our study, wobbling is considered in lumped disturbance.

V. Simulation and Experiment

To initially validate the efficacy of the proposed control method, motion simulations are implemented for both linear and curved paths. Random Gaussian noise is added to the simulations to represent uncertainties, including unmodeled dynamics and time-varying disturbances.

The result of the motion simulation of the linear path is shown in Fig 8. Fig. 8(a) displays the entire motion, while Fig. 8(b) magnifies the motion stabilization process. Fig. 8(c) and (d) show that both position and steering tracking errors remain within a small range and converge nearly to zero. A locally magnified view of the results is also included in the error plot. Our control method reduces overshoot compared to PLOS, and it has a faster response time than PID. Fig. 9 illustrates the curved trajectories of different control methods. As shown in Fig. 9(c) and (d), our proposed combination control method can accurately follow the path with smaller steering adjustments. The outcomes of these simulations provide strong evidence supporting the effectiveness of our proposed control algorithm.

Utilizing the electromagnetic system as described in Section IV, two additional experiments are conducted to evaluate the performance of the proposed algorithm in path following and obstacle avoidance scenarios. In the first scenario, we utilize a transparent circular dish with a 15 mm radius, filled with reverse osmosis water and containing a helical microrobot is placed in the center of the workspace. As the helical microrobots followed the path, the image frames were processed using the standard OpenCV library to collect the position and velocity of each helical microrobot. The imaging system operated at 30 frames per second, ensuring accurate and efficient real-time visual feedback. The implemented automated experimental platform in our study enables the execution of physical experiments with minimal human intervention, thereby minimizing human-induced disturbances to both the robot and the test surfaces. Based on the predefined trajectory, the proposed controller accurately calculates the required current input and transmits instructions to the power supply.

$$\boldsymbol{B} = \boldsymbol{R}\boldsymbol{B}_{ini}$$
$$\mathbf{R} = \begin{bmatrix} \mathbf{C}+\mathbf{A_x^2}(\mathbf{1}-\mathbf{C}) & \mathbf{A_xA_y}(\mathbf{1}-\mathbf{C})-\mathbf{A_z}\mathbf{S} & \mathbf{A_xA_z}(\mathbf{1}-\mathbf{C})+\mathbf{A_y}\mathbf{S} \\ \mathbf{A_xA_y}(\mathbf{1}-\mathbf{C})+\mathbf{A_z}\mathbf{S} & \mathbf{C}+\mathbf{A_y^2}(\mathbf{1}-\mathbf{C}) & \mathbf{A_yA_z}(\mathbf{1}-\mathbf{C})-\mathbf{A_x}\mathbf{S} \\ \mathbf{A_xA_z}(\mathbf{1}-\mathbf{C})-\mathbf{A_y}\mathbf{S} & \mathbf{A_yA_z}(\mathbf{1}-\mathbf{C})+\mathbf{A_x}\mathbf{S} & \mathbf{C}+\mathbf{A_z^2}(\mathbf{1}-\mathbf{C}) \end{bmatrix} \quad (23)$$

Fig. 10 presents the results of curved path following, which records the image of the experiment process. The helical microrobot can be seen moving along the path to the desired position. As shown in Fig. 11, both the position and steering errors converge to within a small neighborhood of zero (1.84 μm and 0.013 rad). To thoroughly examine the inhibitory effect of ESO on disturbances, we conducted an experiment wherein the helical microrobot followed the same path without implementing ESO. The analysis of the results reveals that ESO can effectively reduce the distance error of the helical microrobot by approximately 2 times (see *Supplementary Materials*). The second experiment of the static and dynamic obstacle-avoidance case is shown in Fig. 12 and 13. Firstly, a collision-free initial path was generated in the global map. Then, based on corridor and dynamic constraints, a smooth path was generated. Using the motion control algorithm proposed in this study, the helical microrobot can accurately follow the path, which the average following error is about 3.6 μm. Secondly, when a random obstacle suddenly appeared during the movement, the IAPF method was used to replan the local area path to eventually reach the target point, during the process the microrobot had an average following error of about 6.1 μm. All the experiments can be found in the *Supplementary Video S1*. Additionally, we conducted an experimental setup involving the helical microrobot's obstacle avoidance as the obstacles gradually approached the predefined path. The corresponding results can be found in the *Supplementary Materials*.

VI. Conclusion

In this work, a novel method for the navigation control of magnetic helical microrobots in confined and cluttered environments is proposed. Our path planning method accounts for both global path planning and local emergency replanning. We implement a search-based algorithm with pruning rules to quickly find collision-free waypoints and design an optimal method with spatial and dynamic constraints to generate a smooth global path. To address sudden obstacles that appear in the preset path, we develop an emergency local motion replanning method that integrates velocity gain and potential fields. To achieve high-precision path following, we propose a robust motion control strategy which synergistically integrates both geometric and model-free methods. The tracking control scheme is validated through a combination of simulation and experimental results, which collectively demonstrate its capability to accurately follow arbitrary paths and navigate dynamic environments with micron-level precision. This work demonstrates significant potential for the navigation of magnetic helical microrobots in cluttered and dynamic enclosed environments.

References

[1] L. Yang and L. Zhang, "Motion control in magnetic microrobotics: From individual and multiple robots to swarms," *Annu. Rev. Control, Robot., Auto. Syst.*, vol. 4, no. 1, pp. 509–534, May 2021.

[2] J. Law, J. Yu, W. Tang, Z. Gong, X. Wang, and Y. Sun, "Micro/nanorobotic swarms: From fundamentals to functionalities," *ACS Nano*, vol. 17, no. 14, pp. 12971–12999, Jul. 2023.

[3] J. Miao et al., "Flagellar/ciliary intrinsic driven mechanism inspired all-in-one tubular robotic actuator," *Engineering*, vol. 23, pp. 170–180, Apr. 2023.

[4] Y. Dong, L. Wang, V. Iacovacci, X. Wang, L. Zhang, and B. J. Nelson, "Magnetic helical micro-/nanomachines: Recent progress and perspective," *Matter*, vol. 5, no. 1, pp. 77–109, Jan. 2022.

[5] T. Xu, J. Liu, C. Huang, T. Sun, and X. Wu, "Discrete-time optimal control of miniature helical swimmers in horizontal plane," *IEEE Trans. Autom. Sci. Eng.*, vol. 19, no. 3, pp. 2267–2277, Jul. 2022.

[6] X. Dong, S. Kheiri, Y. Lu, Z. Xu, M. Zhen, and X. Liu, "Toward a living soft microrobot through optogenetic locomotion control of *Caenorhabditis elegans*," *Sci. Robot.*, vol. 6, no. 55, Jun. 2021, Art. no. eabe3950.

[7] J. Liu, T. Xu, S. X. Yang, and X. Wu, "Navigation and visual feedback control for magnetically driven helical miniature swimmers," *IEEE Trans. Ind. Informat.*, vol. 16, no. 1, pp. 477–487, Jan. 2020.

[8] Y. Liu, H. Chen, Q. Zou, X. Du, Y. Wang, and J. Yu, "Automatic navigation of microswarms for dynamic obstacle avoidance," *IEEE Trans. Robot.*, vol. 39, no. 4, pp. 2770–2785, Aug. 2023.

[9] S. Xu, J. Liu, C. Yang, X. Wu, and T. Xu, "A learning-based stable servo control strategy using broad learning system applied for microrobotic control," *IEEE Trans. Cybern.*, vol. 52, no. 12, pp. 13727–13737, Dec. 2022.

[10] J. Liu et al., "3-D autonomous manipulation system of helical microswimmers with online compensation update," *IEEE Trans. Autom. Sci. Eng.*, vol. 18, no. 3, pp. 1380–1391, Jul. 2021.

[11] D. González, J. Pérez, V. Milanés, and F. Nashashibi, "A review of motion planning techniques for automated vehicles," *IEEE Trans. Intell. Transp. Syst.*, vol. 17, no. 4, pp. 1135–1145, Apr. 2016.

[12] J. Chen, T. Liu, and S. Shen, "Online generation of collision-free trajectories for quadrotor flight in unknown cluttered environments," in *Proc. IEEE Int. Conf. Robot. Autom. (ICRA)*, May 2016, pp. 1476–1483, doi: 10.1109/ICRA.2016.7487283.

[13] S. Liu et al., "Planning dynamically feasible trajectories for quadrotors using safe flight corridors in 3-D complex environments," *IEEE Robot. Autom. Lett.*, vol. 2, no. 3, pp. 1688–1695, Jul. 2017.

[14] D. Mellinger and V. Kumar, "Minimum snap trajectory generation and control for quadrotors," in *Proc. IEEE Int. Conf. Robot. Autom.*, Shanghai, China, May 2011, pp. 2520–2525.

[15] Z. Wu, Y. Zhang, Z. Chi, and Q. Xu, "Design and development of a new rotating electromagnetic field generation system for driving microrobots," *IEEE Trans. Magn.*, vol. 58, no. 1, pp. 1–8, Jan. 2022.

[16] D. Lin, W. Chen, K. He, N. Jiao, Z. Wang, and L. Liu, "Position and orientation control of multisection magnetic soft microcatheters," *IEEE/ASME Trans. Mechatronics*, vol. 28, no. 2, pp. 907–918, Apr. 2023.

[17] M. H. D. Ansari et al., "3D printing of small-scale soft robots with programmable magnetization," *Adv. Funct. Mater.*, vol. 33, no. 15, Apr. 2023, Art. no. 2211918.

[18] T. Xu, C. Huang, Z. Lai, and X. Wu, "Independent control strategy of multiple magnetic flexible millirobots for position control and path following," *IEEE Trans. Robot.*, vol. 38, no. 5, pp. 2875–2887, Oct. 2022.

[19] C. Huang, Z. Lai, X. Wu, and T. Xu, "Multimodal locomotion and cargo transportation of magnetically actuated quadruped soft microrobots," *Cyborg Bionic Syst.*, vol. 2022, Jan. 2022, Art. no. 4.

[20] Y. Wang, H. Chen, J. Law, X. Du, and J. Yu, "Ultrafast miniature robotic swimmers with upstream motility," *Cyborg Bionic Syst.*, vol. 4, Jan. 2023, Art. no. 15.

[21] Y. Jia, L. Zheng, D. Dong, Y. Wang, and D. Sun, "Robust navigation control of a microrobot with hysteresis compensation," *IEEE Trans. Autom. Sci. Eng.*, vol. 19, no. 4, pp. 3083–3092, Oct. 2022.

[22] D. Dong, L. Xing, L. Zheng, Y. Jia, and D. Sun, "Automated 3-D electromagnetic manipulation of microrobot with a path planner and a cascaded controller," *IEEE Trans. Control Syst. Technol.*, vol. 30, no. 6, pp. 2672–2680, Nov. 2022.

[23] Y. Kuwata, J. Teo, G. Fiore, S. Karaman, E. Frazzoli, and J. P. How, "Real-time motion planning with applications to autonomous urban driving," *IEEE Trans. Control Syst. Technol.*, vol. 17, no. 5, pp. 1105–1118, Sep. 2009.

[24] G. M. Hoffmann, C. J. Tomlin, M. Montemerlo, and S. Thrun, "Autonomous automobile trajectory tracking for off-road driving: Controller design, experimental validation and racing," in *Proc. Amer. Control Conf.*, Jul. 2007, pp. 2296–2301.

[25] A. Barbot, D. Decanini, and G. Hwang, "Local flow sensing on helical microrobots for semi-automatic motion adaptation," *Int. J. Robot. Res.*, vol. 39, no. 4, pp. 476–489, Mar. 2020.

[26] H. Cao, L. Xing, H. Mo, D. Li, and D. Sun, "Image-guided corridor-based motion planning and magnetic control of microrotor in dynamic environments," *IEEE/ASME Trans. Mechatronics*, vol. 27, no. 6, pp. 5415–5426, Dec. 2022.
[27] J. Liu, T. Xu, and X. Wu, "Model predictive control of magnetic helical swimmers in two-dimensional plane," *IEEE Trans. Autom. Sci. Eng.*, early access, doi: 10.1109/TASE.2023.3250701.
[28] B. Li, T. Acarman, X. Peng, Y. Zhang, X. Bian, and Q. Kong, "Maneuver planning for automatic parking with safe travel corridors: A numerical optimal control approach," in *Proc. Eur. Control Conf. (ECC)*, May 2020, pp. 1993–1998.
[29] P. B. Sujit, S. Saripalli, and J. B. Sousa, "Unmanned aerial vehicle path following: A survey and analysis of algorithms for fixed-wing unmanned aerial vehicless," *IEEE Control Syst. Mag.*, vol. 34, no. 1, pp. 42–59, Feb. 2014.
[30] X. Yan, J. Chen, and D. Sun, "Multilevel-based topology design and shape control of robot swarms," *Automatica*, vol. 48, no. 12, pp. 3122–3127, Dec. 2012.
[31] B.-Z. Guo and Z.-L. Zhao, "Active disturbance rejection control: Theoretical perspectives," *Commun. Inf. Syst.*, vol. 15, no. 3, pp. 361–421, 2015.
[32] Y. Hou et al., "Design and control of a surface-dimple-optimized helical microdrill for motions in high-viscosity fluids," *IEEE/ASME Trans. Mechatronics*, vol. 28, no. 1, pp. 429–439, Feb. 2023.
[33] S. Zhong et al., "Double-modal locomotion of a hydrogel ultra-soft magnetic miniature robot with switchable forms," *Cyborg Bionic Syst.*, early access, 2023, doi: 10.34133/CBSYSTEMS.0077.

Shihao Zhong received the B.S. degree in automation from the North China University of Technology, Beijing, China, in 2021. He is currently pursuing the Ph.D. degree in mechanical engineering with the Beijing Institute of Technology, Beijing.

His research interests include navigation control of micro-/nanomachines.

Yaozhen Hou received the B.S. degree in mechatronics and the Ph.D. degree in mechanical engineering from the Beijing Institute of Technology, Beijing, China, in 2017 and 2023, respectively.

He has been a Post-Doctoral Scientist of Mechanical Engineering with the Beijing Institute of Technology, since 2023. His research interests include micro/nano manupulation.

Qing Shi (Senior Member, IEEE) received the B.S. degree in mechatronics from the Beijing Institute of Technology, Beijing, China, in 2006, and the Ph.D. degree in biomedical engineering from Waseda University, Japan, in 2012.

He was a Research Associate with GCOE, Global Robot Academia, Waseda University, from 2009 to 2013. He is currently a Professor with the School of Mechatronical Engineering, Beijing Institute of Technology. His research interests include bio-inspired robots, computer vision, and micro/nano robotics.

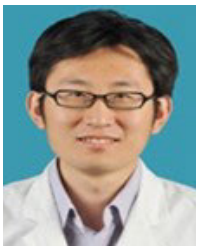

Yang Li received the master's degree in health management and the master's degree in Chinese medicine from the Beijing University of Chinese Medicine, Beijing, China, in 2007 and 2010, respectively.

He has been an Associate Researcher with Peking University First Hospital, since 2018. His research interests include medical technology, medical cooperation, and hospital management.

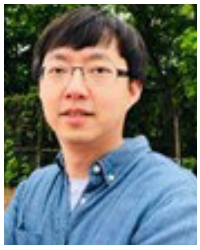

Hen-Wei Huang received the B.S. and M.S. degrees in mechanical engineering from National Taiwan University, Taiwan, in 2011 and 2012, respectively, and the Ph.D. degree in robotics technology from ETH Zürich, in 2018.

He is currently an Assistant Professor of Medicine with the Harvard Medical School. His research interests include in vivo wireless sensor networks, personalized medicine, controlled drug delivery, robotics, and translational medicine.

Qiang Huang (Fellow, IEEE) was a Research Fellow with the National Institute of Advanced Industrial Science and Technology, Tokyo, Japan, from 1996 to 1999. He was a Research Fellow with the University of Tokyo, from 1999 to 2000. He is currently a Professor with the Beijing Institute of Technology, Beijing, China. He is the Director of the Key Laboratory of Biomimetic Robots and Systems, Ministry of Education of China.

He received the First Class Prize of the Ministry of Education Award for Technology Invention. He serves as the Chair for many IEEE conferences, such as the Organizing Committee Chair for the 2006 IEEE/RSJ International Conference on Intelligent Robots and Systems and the General Chair for the 2017 IEEE International Conference on Robotics and Biomimetics and the 2018 IEEE-RAS International Conference on Humanoid Robots.

Toshio Fukuda (Life Fellow, IEEE) received the B.S. degree from Waseda University, Tokyo, Japan, in 1971, and the M.S. and Ph.D. degrees from the University of Tokyo, Tokyo, in 1973 and 1977, respectively.

From 1977 to 1982, he was with the National Mechanical Engineering Laboratory, Tsukuba, Japan. From 1982 to 1989, he was with the Tokyo of University Science. Since 1989, he has been with Nagoya University, Nagoya, Japan, where he was a Professor with the Department of Micro System Engineering, and a Professor with Meijo University, Nagoya. He is currently a Professor (1000 Foreign Experts Plan) with the Intelligent Robotics Institute, School of Mechatronic Engineering, Beijing Institute of Technology, Beijing, China, where he is mainly engaged in the research fields of intelligent robotic systems, cellular robotic systems, mechatronics, and micro/nano robotics.

Dr. Fukuda was the President of the IEEE Robotics and Automation Society (1998–1999), the Editor-in Chief of IEEE/ASME TRANSACTIONS ON MECHATRONICS (2000–2002), the Director of the Division X: Systems and Control (2001–2002), the IEEE Founding President of the Nanotechnology Council (2002–2003, 2005), the Director Region 10 (2013–2014), and the Director of the Division X: Systems and Control (2017–2018).

Huaping Wang (Member, IEEE) received the B.S. degree in mechatronics and the Ph.D. degree in mechanical engineering from the Beijing Institute of Technology, Beijing, China, in 2010 and 2015, respectively.

He has been a Professor with the Beijing Institute of Technology, since 2022. His research interests include micro-nano robotics, micro-nano manipulation, and automation at micro-nano scales.